AIP | Journal of Applied Physics

Temporal evolution of the laser-induced plasma generated by IR CO2 pulsed laser on carbon targets

J. J. Camacho, L. Díaz, M. Santos, L. J. Juan, and J. M. L. Poyato

Citation: J. Appl. Phys. 106, 033306 (2009); doi: 10.1063/1.3190542
View online: http://dx.doi.org/10.1063/1.3190542
View Table of Contents: http://jap.aip.org/resource/1/JAPIAU/v106/i3
Published by the American Institute of Physics.

Temporal evolution of the laser-induced plasma generated by IR CO_2 pulsed laser on carbon targets

J. J. Camacho,[1,a)] L. Díaz,[2] M. Santos,[2] L. J. Juan,[1] and J. M. L. Poyato[1]
[1]*Departamento de Química-Física Aplicada, Facultad de Ciencias, Universidad Autónoma de Madrid, Cantoblanco, 28049 Madrid, Spain*
[2]*Instituto de Estructura de la Materia, CFMAC, CSIC, Serrano 121, 28006 Madrid, Spain*

(Received 22 May 2009; accepted 2 July 2009; published online 5 August 2009)

Time-resolved optical emission analysis was carried out for the plasma plume, produced by high-power tunable IR CO_2 pulsed laser ablation of graphite, at $\lambda = 10.591$ μm and in a regime of relatively high laser fluences (123–402 J/cm^2). Wavelength-dispersed spectra of the plasma plume, at medium-vacuum conditions (4 Pa) and at 9.0 mm from the target, show ionized species (C^+, C^{2+}, C^{3+}, C^{4+}, N_2^+, N^+, and O^+), neutral atoms (C, H, N, and O), and neutral diatomic molecules (C_2, CN, OH, CH, and N_2). In this work, we focus our attention on the temporal evolution of different atomic/ionic and molecular species over a broad spectral range from 190 to 1000 nm. The results show a faster decay for ionic fragments than for neutral atomic and molecular species. The velocity and kinetic energy distributions for different species were obtained from time-of-flight measurements using time-resolved optical emission spectroscopy. Possible mechanisms for the production of these distributions are discussed. Excitation temperature, electron density, and vibrational temperature in the laser-induced plasma were estimated from the analysis of spectral data at various times from the laser pulse incidence. © *2009 American Institute of Physics*. [DOI: 10.1063/1.3190542]

I. INTRODUCTION

When a powerful focused laser beam interacts with a target, an intense plasma or spark (brilliant flash) is created. This laser-induced breakdown (LIB) region develops a shock wave into the ambient medium. Laser ablated plasmas are currently a topic of considerable interest. Pulsed laser ablation (PLA) of graphite is an effective method for the production of a wide variety of carbon-related materials such as diamondlike carbon, carbon nanotubes, carbon nitride, and high fullerene carbon molecules.[1–7] The structure and properties of the prepared materials depend strongly on the conditions under which the graphite target is ablated and the materials are prepared. In this way, information on the progress of the plasma plume and the transport of the ablated species will be of significant importance in understanding the mechanisms of deposited films. Due to the many experimental parameters involved in the PLA, an exhaustive investigation of the plasma plume would involve the processing of an impressive number of records. To investigate the plume expansion process and gas-phase reactions, several diagnostic techniques have been employed in the past years. Because of the transient features of the plume created by PLA, optical emission spectroscopy (OES) technique with time and space resolution is especially appropriate to obtain information about the behaviors of the ablation created species in space and time as well as the dynamics of the plume evolution. This technique with temporal resolution has been used by many researchers to investigate the graphite ablation plume.[8–25] The wavelength and spatially resolved measurements of emission spectra of the CO_2 laser ablation plume at the carbon target have been reported recently by us.[26,27]

The present paper is aimed at discussing thermochemical processes produced by a high-power IR CO_2 pulsed laser on graphite target and at evaluating laser ablation induced changes, which are of fundamental importance in establishing the mechanisms responsible for the plasma emission. In this work we present some new results obtained from the time-resolved spectroscopic analysis of the PLA plume. We discuss the dynamics of the plume expansion and formation of different atomic, ionic, and molecular species for different delay times with respect to the beginning of the laser pulse. The velocity and kinetic distributions for different species (C, C^+, C^{2+}, C^{3+}, C_2, CN, and N_2^+) were obtained from the time-of-flight (TOF) measurements using time-resolved OES. Line intensities from single ionized carbon were used for determining electron temperature, and Stark-broadened profiles of some lines were employed to calculate electron density. Estimates of excitation and vibrational temperatures and electron density are reported at various times elapsed after firing the laser pulse. Although OES gives only partial information about the plasma particles, this diagnostic technique helped us to draw a picture of the plasma in terms of the emitting chemical species, to evaluate their possible mechanisms of excitation and formation, and to study the role of gas-phase reactions in the plasma expansion process.

II. EXPERIMENTAL

The experimental setup used in this study is presented in Fig. 1, and has been partially described in Refs. 26 and 27. A transverse excitation atmospheric (TEA)-CO_2 laser (Lumonics model K-103) operating on an 8:8:84 mixture of

[a)]FAX: +34914974512. Electronic mail: j.j.camacho@uam.es.

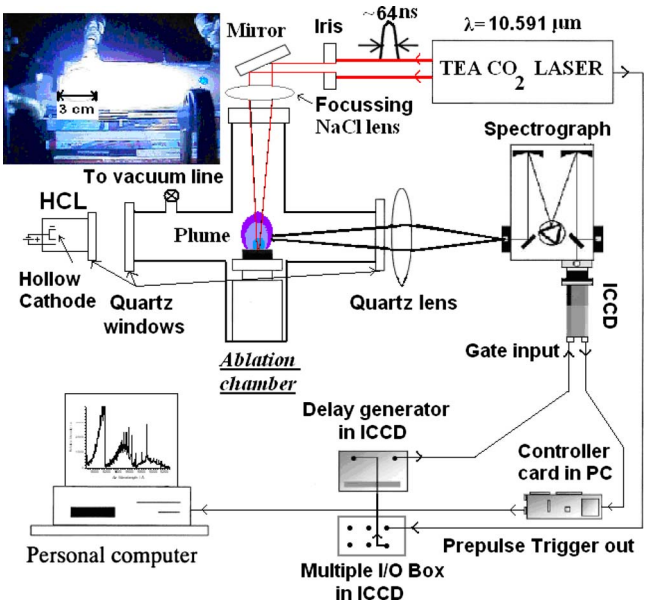

FIG. 1. (Color online) Schematic of the experimental setup of the time gated ICCD for PLA diagnostics.

CO_2:N_2:He, respectively, was used in the experiment. The CO_2 laser irradiation of carbon target was carried out using the 10P(20) line at $\lambda = 10.591$ μm. The temporal shape of the TEA-CO_2 laser pulse (see Fig. 2), monitored with a photon drag detector (Rofin Sinar 7415), consisted in a prominent spike of a full width at half maximum (FWHM) ~64 ns followed by a long lasting tail of lower energy and about 3 μs duration. The primary laser beam was angularly defined and attenuated by a diaphragm of 17.5 mm diameter before entering to the cell. The pulsed CO_2 laser beam was perpendicularly focused with a NaCl lens of 24 cm focal length onto the target surface. The CO_2 laser energy was measured in front of the lens with a Lumonics 20D pyroelectric detector through a Tektronix TDS 540 digital oscilloscope. The focused radius of the laser beam was measured at the target position with a pyroelectric array detector Delta Development Mark IV. The measured focused-spot area was 7.85×10^{-3} cm^2. The measured maximum laser energy was 3160 mJ, leading to an estimated power of 49.5 MW, intensity (power density or irradiance) of 6.31 GW cm^{-2}, fluence of 402 J cm^{-2}, photon flux of 3.4×10^{29} photon cm^{-2} s^{-1}, and electric field of 1.63 MV cm^{-1} on the target surface. The laser intensity was varied using several calibrated CaF_2 attenuators. The high purity graphite target (~99.99%) was placed in a low-vacuum Pyrex cell of 4.5 cm diameter and 43 cm length equipped with a NaCl window for the laser beam and two quartz windows for optical access. The cell was evacuated with the aid of a rotary pump, to a base pressure of 4 Pa that was measured by a mechanical gauge. The light emitted from the laser-induced plasma was optically imaged 1:1, at right angles to the normal of the target surface, by a quartz lens (focal length 4 cm, f-number=$f/2.3$) onto the entrance slit of the spectrometer. The distance between the plasma axis and the entrance slit was 16 cm.

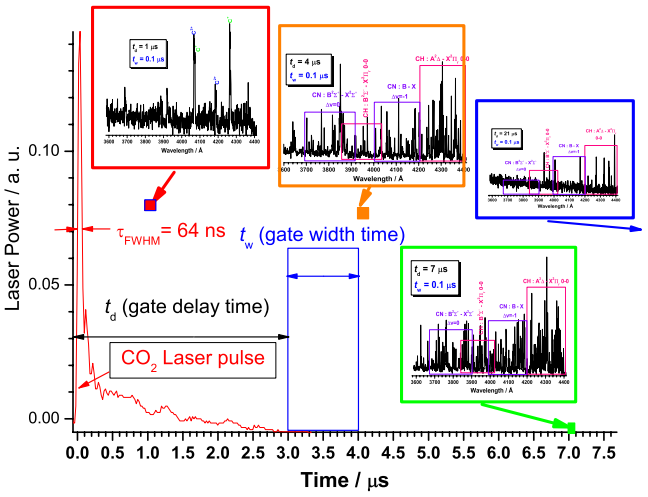

FIG. 2. (Color online) A schematic overview of the temporal history of LIB carbon plasma. Here t_d is the gate delay time and t_w is the gate width time during which the plasma emission is monitored. The inserts illustrate some spectra observed at different delay and width times. The temporal shape of the CO_2 laser pulse (recorded with the aid of the photon drag detector) is also shown.

Two spectrometers were used: a 1/8 m Oriel spectrometer (10 μm slit and grating of 1200 grooves mm^{-1}) in the spectral region 2000–10 500 Å at a resolution of ~1.3 Å in first order; and a 0.32 m ISA Jobin Yvon Spex (model HR320) spectrometer (adjustable slit and holographic grating of 2400 grooves mm^{-1}) in the spectral region 1900–7500 Å at a resolution of ~0.10 Å in first order. A 1024×1024 matrix of 13×13 μm^2 individual pixels intensified charge-coupled device (ICCD) (Andor iStar DH-734), with thermoelectric cooling working at −20 °C, was attached to the exit focal plane of the spectrographs and used to detect the optical emissions from the laser-induced plasma. For synchronization, the CO_2 laser was operated at the internal trigger mode and the ICCD detector was operated in external and gate modes. The external trigger signal generated by the laser was fed directly into the back of the ICCD detector head. The total insertion delay (or propagation delay) is the total length of time taken for the external trigger pulse to travel through the digital delay generator and gater so that the ICCD will switch on. This insertion delay time was 45 ± 2 ns. The time jitter between the laser and the fast ICCD detector gate was about ± 2 ns. The delay time t_d is the time interval between the arrival of the laser pulse on the target and the activation of the ICCD detector. The gate width delay time t_w is the time interval during which the plasma emission is monitored by the ICCD. Both parameters were adjusted by the digital delay generator of the ICCD detector (see Fig. 2). The square box represents the gate width time t_w. The resolution of the gate pulse delay time and the gate pulse width time was 25 ps. The CO_2 laser pulse picked up with the photon drag detector triggered a Stanford DG 535 pulse generator through the scope and this pulse was used as an external trigger in the ICCD camera. The laser pulse and the gate monitor output were displayed in a Tektronix TDS 540 digital oscilloscope. In this way, by using the output of the photon drag detector, the Tektronix TDS 540 digital oscilloscope, the Stanford DG 535 delay pulse gen-

erator, and the gate monitor output of the ICCD camera, the gate width time t_w and the gate delay time t_d could be adjusted without insertion time.

The intensity response of the detection system was calibrated with a standard (Osram No. 6438, 6.6 A, 200 W) halogen lamp and Hg/Ar pencil lamp. Several (Cu/Ne, Fe/Ne, and Cr/Ar) hollow cathode lamps (HCLs) were used for the spectral wavelength calibration of the spectrometers.

III. RESULTS AND DISCUSSION

When a high-power laser pulse is focused on a solid surface the target becomes ablated. If the laser irradiance in the focal volume surpasses the breakdown threshold of the system formed by the vaporized atoms and residual gas, a breakdown, characterized by a brilliant flash of light accompanied by a distinctive cracking noise, is produced. At the top of Fig. 1 we show an image of LIB plasma in graphite induced by a single CO_2 laser pulse. The plume size length was around 14 cm. The laser was focused on a point at the center of the target. The observations of the LIB geometry during the experiments indicate that the actual plasma region was not entirely spherical, but slightly elongated in the direction of the laser beam propagation. The CO_2 laser pulse remains in the focal volume after the plasma formation for some significant fraction of its duration and the plasma formed can be heated to very high temperatures and pressures by inverse bremsstrahlung absorption. Since plasmas absorb radiation much more strongly than ordinary mater, plasmas can block transmission of incoming laser light to a significant degree; a phenomenon known as "plasma shielding."[28] The high temperatures and pressures produced by plasma absorption can lead to thermal expansion of the plasma at high velocities, producing an audible acoustic signature, shock waves, and cavitation effects. The plasma also tends to expand back along the beam path toward the laser, a phenomenon known as "moving breakdown." The shock wave heats up the surrounding gas, which is instantaneously transformed in strongly ionized plasma.

A. Time-resolved emission spectra for laser-induced carbon plasma

All the experimental measurements were taken with the carbon target at the focal point of the NaCl lens and focusing the plasma plume at a constant distance of 9.0 mm from the target surface along the plasma expansion direction. Each firing of the laser produces a single LIB spectrum. Two different types of spectra were recorded: time integrated and time resolved. In the acquisition of time-integrated spectra, a good signal-to-noise ratio has been obtained averaging each spectrum over several successive laser pulses. Typically the signals from 20 laser pulses were averaged and integrated over the entire emission time. In time-resolved measurements, the delay t_d and width t_w times were varied. It was verified that the plasma emission was reproducible over more than seven ablation events by recording the same spectrum several times. The temporal history of LIB carbon plasma is illustrated schematically in Fig. 2. The time for the beginning of the CO_2 laser pulse was considered as the origin of the time scale ($t=0$). Inserts illustrate some emission spectra recorded at different delay and width times. The temporal shape of the CO_2 laser pulse is also shown.

The LIB spectra of carbon were measured at different delay and width times. In a first set of experimental measurements, the spectra were obtained at low resolution in the spectral region 200–1000 nm. These spectra (not shown) reproduce particular emission of carbon plasma in a medium-vacuum air atmosphere.[26,27] From all these spectra we can observe that the intensity of ionic species (C^+, C^{2+}, C^{3+}, N^+, and O^+) increases up to ~ 1 μs and decays rapidly at high delay times. Above ~ 4 μs these species are not observed. The band emission of molecular species as C_2, CN, and OH slightly increase up to ~ 4 μs and decrease for high delay time, being observed up to ~ 15 μs in accordance with the molecule. On the other hand we can see that the line intensity of atomic carbon increases up to ~ 1 μs and slowly decays at high delay times, being observed up to ~ 30 μs.

In order to get more insight into laser ablation of graphite and to understand the LIB dynamics, we have scanned in the UV-visible spectral region with higher resolution (see Sec. II). As an example some results for the spectral region 4640–4750 Å are shown in Figs. 3–5. Figures 3(a) and 3(b) compare two high-resolution spectra. The spectral range was chosen in order to detect both double and triple ionized carbon species and C_2 diatomic molecule. The data acquisition was performed by averaging the signal over (a) 20 successive laser shots ($t_d=0$ μs and $t_w \gg 30$ μs) and (b) 7 successive laser shots ($t_d=4$ μs and $t_w=0.02$ μs). The intensities of the emission of ionized $C^{2+}(1s^2 2s 3p\ ^3P^0_{2,1,0} \rightarrow 1s^2 2s 3s\ ^3S_1)$ around 4650 Å, and C^{3+} around 4658.3 Å are considerably higher, in the spectrum of Fig. 3(a), than the C_2 $(d-a)$ swan $\Delta v=+1$ sequence emission. On the other hand, the intensities of the C_2 $(d-a)$ swan $\Delta v=+1$ sequence are similar in both experiments [Figs. 3(a) and 3(b)]. Figures 4 and 5 show the typical temporal sequence of laser-induced carbon plasma. At early times ($t_d \leq 0.02$ μs) emissions from C^{2+} and C^{3+} are easily detected between 4645 and 4670 Å [see inset within Fig. 4(a)]. As seen in Fig. 4(b) during the initial stages after the laser pulse ($t_d \leq 0.04$ μs), C^{2+} emissions dominate the spectrum. As time evolves (0.04 μs $\leq t_d \leq 1.5$ μs), C^{3+} emissions dominate the spectrum. As the delay is increased up to 2.5 μs (1.5 μs $\leq t_d \leq 2.5$ μs) again C^{2+} emissions dominate the spectrum. These ionic lines decrease quickly for higher delay times, being detected up to ~ 3 μs. Some oxygen and nitrogen ionic lines were also observed in the spectra at the gate delay from 0.02 to 1 μs and its emission intensities remain approximately constant in this time interval [see Fig. 4(a)]. They vanish after a delay of ~ 1.5 μs. This shows that the air was ionized by the CO_2 laser pulse and by the collisions with the laser-induced plasma. During the time period up to ~ 0.5 μs, no apparent C_2 emissions were observed. As can be seen from Fig. 5, the C_2 $(d-a;\ \Delta v=1$ band sequence) emissions were clearly observed from ~ 2 μs. The C_2 emission intensities increase lightly with increasing t_d, reach a maximum at ~ 5 μs, and then decrease as the time is further increased.

Figure 6 displays the temporal evolution of the LIB plasma in the spectral region 2425–2570 Å. At early times

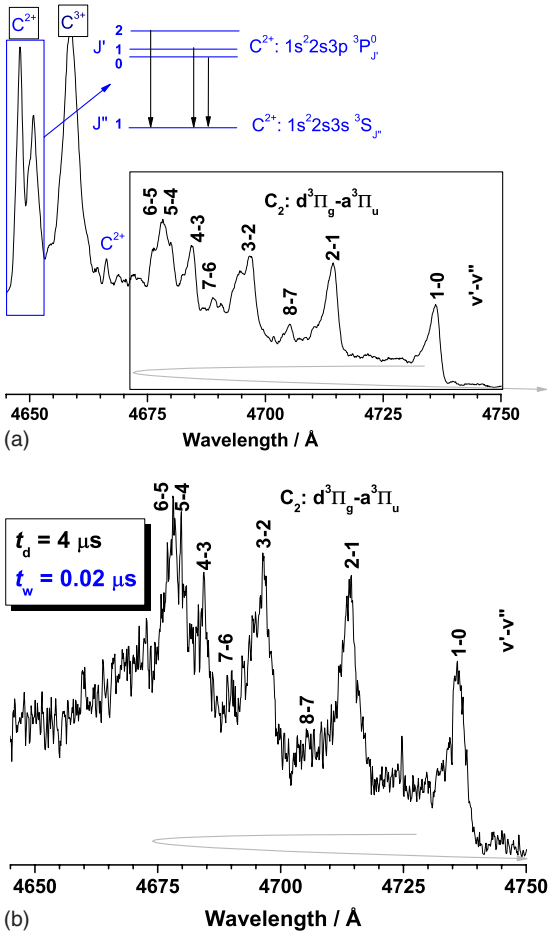

FIG. 3. (Color online) [(a) and (b)] Measured high-resolution PLA (402 J/cm^2) of graphite emission spectra observed in the region 4645–4750 Å. The data acquisition was performed by averaging the signal over (a) 20 successive laser shots with t_d=0 μs and $t_w \gg 30$ μs, and (b) 7 successive laser shots with t_d=4 μs and t_w=0.02 μs. The assignments of some ionic lines of C^{2+} and C^{3+} and molecular bands of C_2 are indicated. The insert in (a) illustrates the angular spin-orbit structure of one triplet of C^{2+} line.

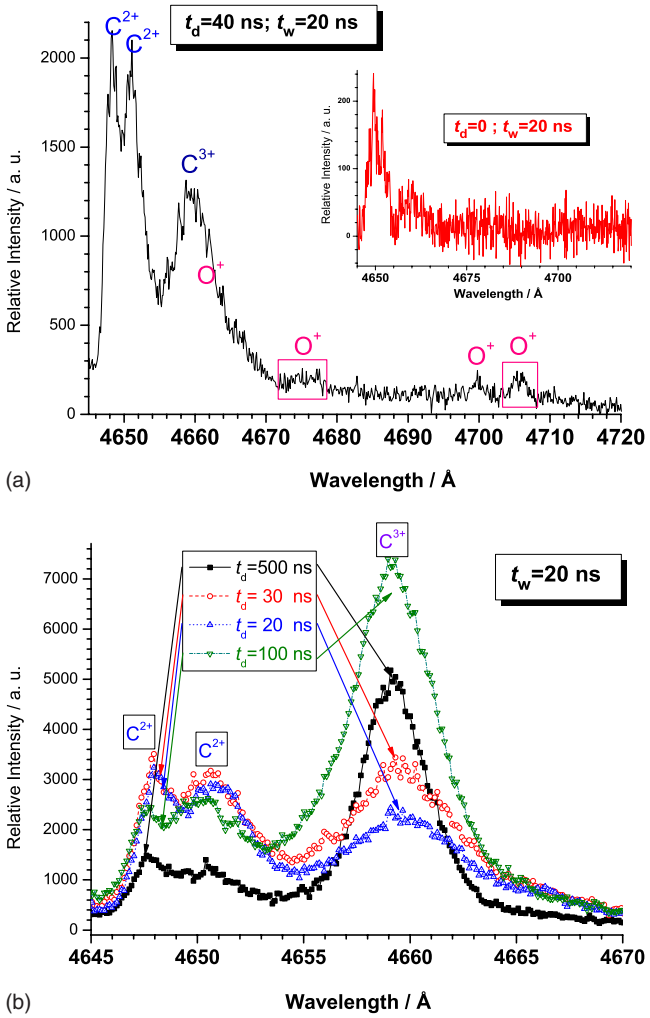

FIG. 4. (Color online) [(a) and (b)] Time-resolved high-resolution emission spectra from laser-induced carbon plasma (402 J/cm^2) observed in the regions (a) 4645–4720 Å monitored at 40 ns delay time and (b) 4645–4670 Å monitored at 20, 30, 100, and 500 ns gate delay times for a fixed gate width time of 20 ns. The inset in (a) displays the spectrum of the first 20 ns after incidence of the laser pulse.

($t_d < 2$ μs), the predominant emitting species are $C[2s^2 2p(^2P^0)3s\ ^1P_1^0 \rightarrow 2s^2 2p^2\ ^1S_0]$ resonance line at 2478.6 Å, $C^+(2p^3\ ^2D^0_{3/2,5/2} \rightarrow 2s2p^2\ ^2P_{1/2,3/2})$ with two lines at 2509.1 and 2512.1 Å, and C^{3+} with lines at 2524.4 and 2530.0 Å. The spectra were recorded with a gate width of 20 ns. One can see that immediately after the peak laser pulse ($t_d < 0.1$ μs), the plasma emission spectrum consists in the previously mentioned weak lines of C, C^+, and C^{3+}, which increase with time. When the delay ($0.1 \leq t_d \leq 1$ μs) increases such lines steeply enhance as a consequence of the expansion and heating of the plasma. At longer times ($1 < t_d < 4$ μs), the ion lines of C^+ and C^{3+} significantly decrease in intensity as a consequence of the expansion and cooling of the plasma plume and its recombination into ground state ions. At longer times ($t_d > 4$ μs) the carbon ionic lines disappear while the C neutral line becomes stronger and then decays over a much longer period.

Figure 7 shows time-resolved OES from laser-induced carbon plasma observed in the region 3830–3960 Å monitored at 10, 3, 0.5, 0.05, and 0 μs gate delays for a fixed gate width time of 20 ns and time-integrated spectrum (t_d=0 μs and $t_w \gg 40$ μs). This last time-integrated spectrum was averaged over 20 laser pulses in order to reduce standard deviation. At early times ($t_d < 0.5$ μs), the predominant emitting species are several lines of C^+ and the $v'=0-v''=0$ band of N_2^+ ($B\ ^2\Sigma_u^+$-$X\ ^2\Sigma_g^+$) at ~3915 Å. Also a very weak emission from CN ($B\ ^2\Sigma^+$-$X\ ^2\Sigma^+$; $\Delta v=0$ sequence) is observed. At t_d=0.5 μs, the 0-0 band of N_2^+ practically disappears. When the delay increases ($0.5 \leq t_d \leq 3$ μs), the emission intensities of CN rovibrational lines are slightly enhanced as a consequence of the expansion and heating of the plasma. At longer times ($t_d > 3$ μs), the ion lines of C^+ significantly decrease in intensity as a consequence of the expansion and cooling of the plasma plume and its recombination into ground state ions. Moreover, the CN molecular bands decrease being observed up to ~12 μs.

Figure 8 shows time-resolved OES from laser-induced carbon plasma observed in the region 5090–5190 Å monitored at 0, 1, 3, 4, and 10 μs gate delays for a fixed gate width time of 20 ns and time-integrated spectrum (t_d=0 μs and $t_w \gg 40$ μs). This last time-integrated spectrum was averaged over 20 laser pulses. At early times ($t_d < 3$ μs), the

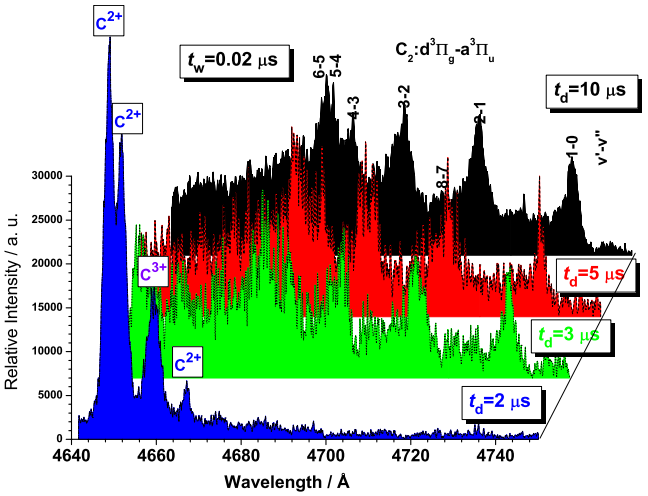

FIG. 5. (Color online) Time-resolved high-resolution emission spectra from laser-induced carbon plasma (402 J/cm^2) observed in the region 4645–4750 Å monitored at 2, 3, 5, and 10 μs gate delays for a fixed gate width time of 20 ns.

predominant emitting species is C^+ detected by several lines. Also a very weak emission from C_2 ($d\,^3\Pi_g$-$a\,^3\Pi_u$; $\Delta v=0$ sequence) is observed. At $t_d \sim 4$ μs, the C^+ lines practically disappear. When the delay ($0.5 \leq t_d \leq 4$ μs) increases C_2 rovibrational lines enhance. At longer times ($t_d > 4$ μs), the C_2 rovibrational lines decrease, being observed up to ~ 15 μs.

B. TOF and velocity

Space- and time-resolved OES measurements could be used to estimate plasma expansion rate. To obtain additional time-resolved information about the optical emission of the plasma, resolved spectra have been recorded at different delay times at a distance of 9.0 mm from the carbon target. The temporal evolution of spectral atomic, ionic, and molecular line intensities at a constant distance from the target can be used to construct the TOF profile. TOF studies of the emission provide fundamental information regarding the time taken for a particular species to evolve after the laser-induced plasma has been formed. Specifically, this technique gives an indication of the velocity of the emitted species.[29] A rough estimation of the velocity for the different species in the plume can be inferred from the time-resolved spectra by plotting the intensities of selected emission lines versus the delay time, and then calculating the velocity by dividing the distance from the target by the time where the emission peaks. This method for the determination of plasma velocity should be used with care due to the superposition of both expansion and forward movements of the plasma plume. We assume a plasma model consisting of two plasmas:[30] a primary plasma that acts as an initial explosion energy source and emits an intense continuum emission background for a short time just above the surface of the target, and a secondary plasma that expands with time around the primary plasma. The secondary plasma is formed by excitation from the shock wave, emitting atomic, ionic, and molecular bands with low background signal. Taking into account the distance

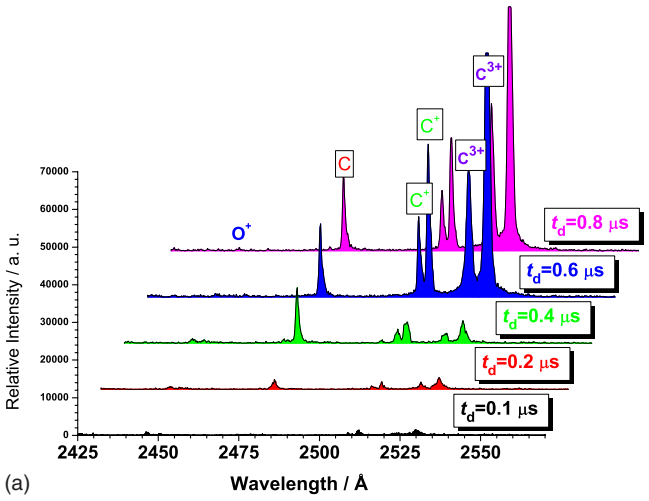

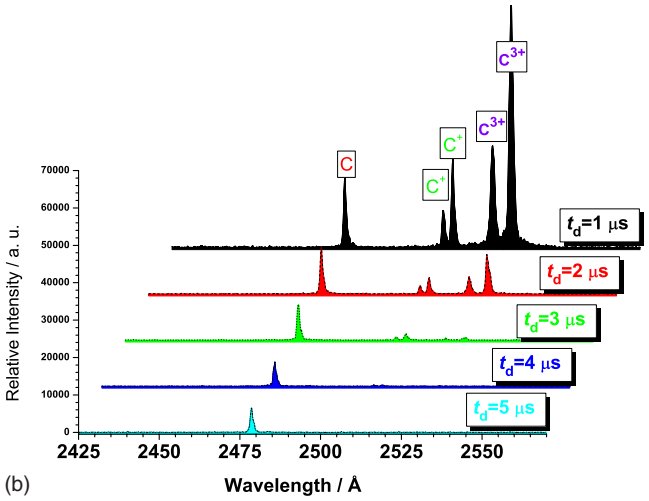

FIG. 6. (Color online) Time-resolved high-resolution emission spectra from laser-induced (402 J/cm^2) carbon plasma observed in the region 2425–2570 Å monitored at 0.1, 0.2, 0.4, 0.6, 0.8, 1, 2, 3, 4, and 5 μs gate delays for a fixed gate width time of 20 ns.

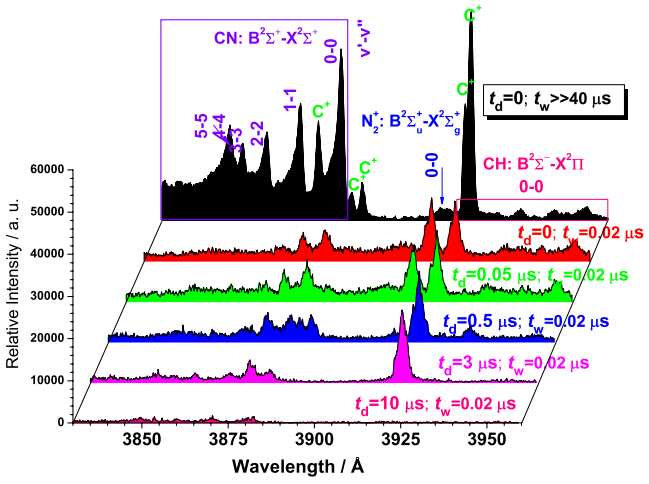

FIG. 7. (Color online) Time-resolved high-resolution emission spectra from laser-induced (402 J/cm^2) carbon plasma observed in the region 3830–3960 Å monitored at 10, 3, 0.5, 0.05, and 0 μs gate delays for a fixed gate width time of 20 ns and time-integrated spectrum ($t_d=0$ μs and $t_w \gg 40$ μs).

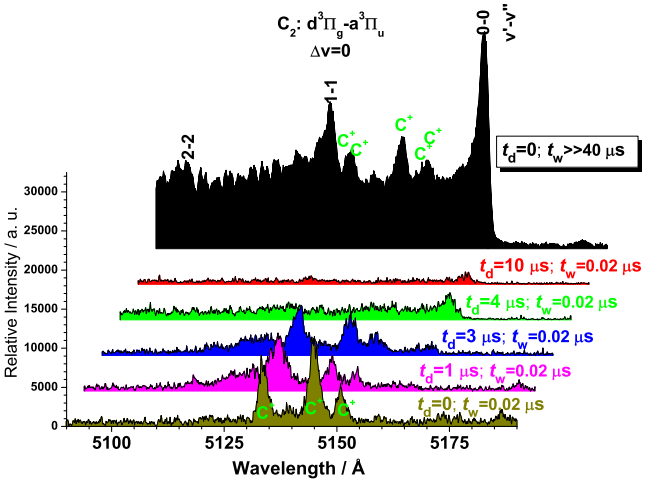

FIG. 8. (Color online) Time-resolved high-resolution emission spectra from laser-induced (402 J/cm^2) carbon plasma observed in the region 5090–5190 Å monitored at 0, 1, 3, 4, and 10 μs gate delays for a fixed gate width time of 20 ns and time-integrated spectrum (t_d=0 μs and $t_w \gg 40$ μs).

of our measurements (9 mm) we study the velocity of species in the expansion of the secondary plasma.

Figure 9(a) displays the normalized TOF profile for the ablation experiments induced by CO_2 laser pulses as indicated in Sec. II, of C, C^+, and C^{3+} line intensities in the UV region and C^{2+} in the visible region. In these experimental TOF distributions $N(t)$ are essentially number density distributions. They were converted to flux distributions dN/dt by employing a correction factor z/t, where z means the flight distance (z=9 mm) and t is the delay time after the ablation laser pulse. From the TOF spectra, the translational kinetic energy can be deduced [KE=$(1/2)m(z/t)^2$] by measuring the flight time t required to transverse the distance from the target to the detector z. It should be mentioned that the estimation of velocity distributions assumes that the emitting species are generated on the target. The kinetic energy distributions obtained for some species are plotted in the inset of Fig. 9(a). In a first approximation, we can consider that the maxima in the velocity distribution represent the average velocities. From these values, the average kinetic energy can be estimated. The velocity distribution, in a more accurate way, can be fitted to a superposition of terms of the flux-weighted Maxwell–Boltzmann function.[29] By using the first approximation, we have observed large atomic and ion average kinetic energies. The velocity distributions that are derived from these TOF distributions are displayed in Fig. 9(b). At the laser fluence used in this series of experiments (402 J/cm^2), TOF distributions present different characteristics. Thus, the velocity distributions of carbon ionic species C^+, C^{2+}, and C^{3+} are comparatively more narrow [~12.6, ~13.6, and ~10 km/s (FWHM), respectively] than the velocity distribution of carbon neutral species [~24.7 km/s (FWHM)]. The velocity distributions of carbon species C, C^+, C^{2+}, and C^{3+} are centered at about 11.2, 14.5, 14.5, and 12.9 km/s, respectively, and mainly the C^{3+} species shows two main components, with most probable velocities of approximately 8.1 and 12.7 km/s. On the other hand, the ionic species show that their velocity distributions are peaked at ~12.9–14.5 km/s, higher than those corresponding to the

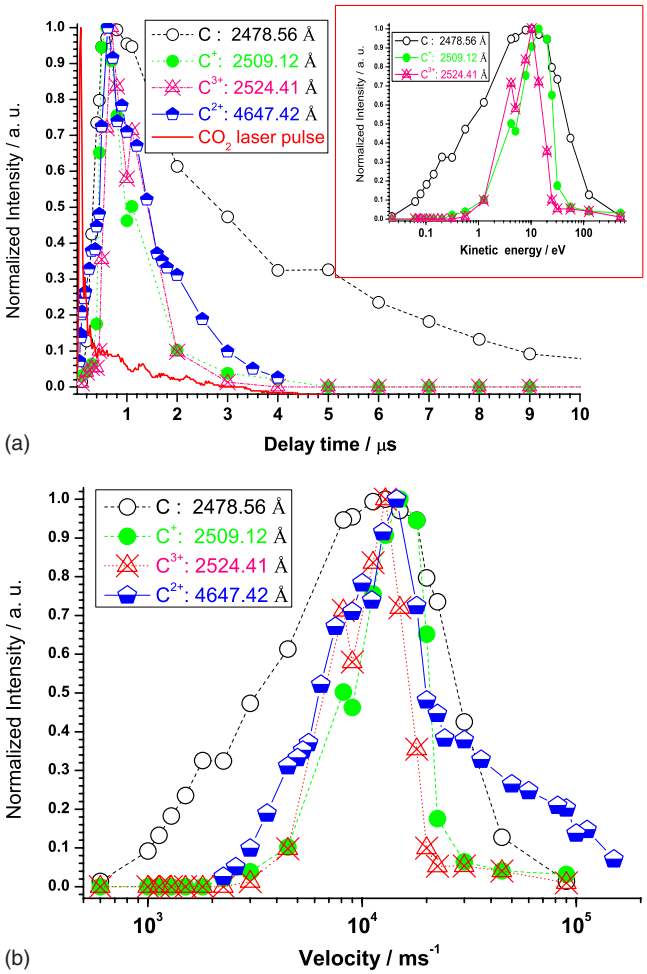

FIG. 9. (Color online) (a) Normalized number density TOF distributions for C (2478.56 Å), C^+ (2509.12 Å), C^{2+} (4647.42 Å), and C^{3+} (2524.41 Å) lines and temporal profile of the TEA-CO_2 laser pulse as a function of delay time (fixed gate width time of 20 ns) for a laser fluence of 402 J/cm^2. The inset plot shows the kinetic energy distribution of several species derived from TOF spectra; (b) velocity distributions derived from the experimental TOF profiles for the indicated species.

carbon neutral species ~11.2 km/s but much narrow. In Fig. 9 it is also observed that atomic C lasts more (>12 μs) than ionic species possibly due to the less energy necessary for its formation taking advantage of the pulse tail and also to the continuous recombination of ions with electrons to give excited carbon. The different components of the velocity distributions for each species can be due to the different formation mechanisms. Particularly, for C^{2+} species [Fig. 9(b)], the complex velocity distribution observed might indicate that several processes can be involved in its formation [$C+nh\nu+e^- \rightarrow C+e^{-*} \rightarrow C^{2+}+3e^-$ (inverse bremsstrahlung and electron-impact ionization), $C^+ + e^{-*} \rightarrow C^{2+}+2e^-$ (electron-impact ionization), $C^{3+}+e^- \rightarrow C^{2+}$ (recombination), etc.].

Figure 10 displays the TOF profiles and velocity distributions for the ablation experiments induced by CO_2 laser pulses (402 J/cm^2) of N_2^+ (0-0; 3913 Å), C^+ (3920.69 Å), CN (0-0; 3882 Å), and C^+ (3875.68 Å) species as a function of the delay time. We notice the appearance of a strong maximum for all species for a delay of 0.1 μs in the emission intensity distribution. The C^+ and N_2^+

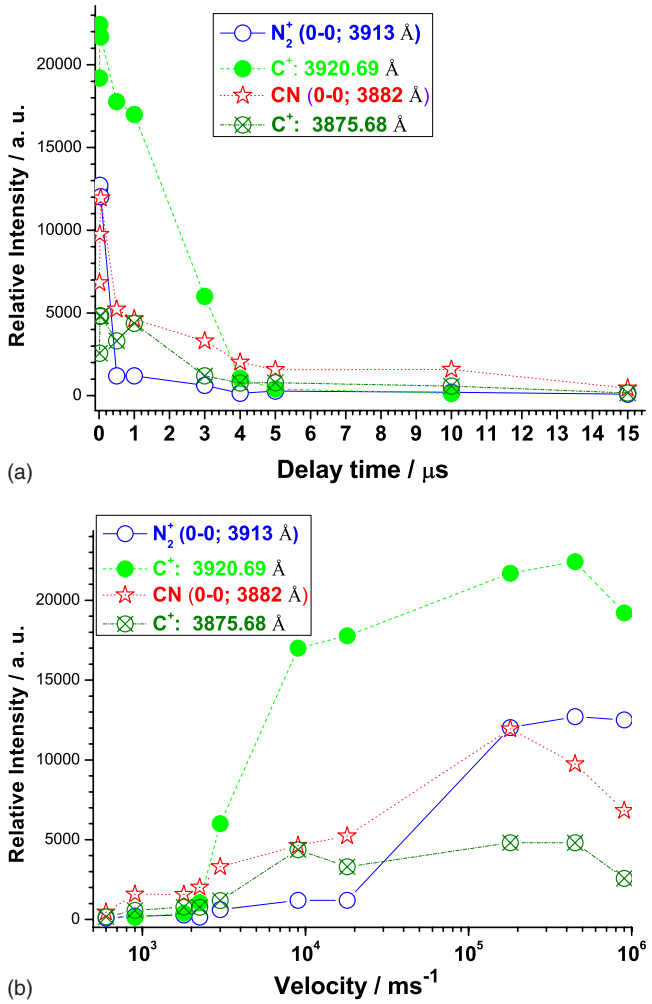

FIG. 10. (Color online) (a) Number density TOF distributions for N_2^+ (0-0; 3913 Å) , C^+ (3920.69 Å), CN (0-0; 3882 Å), and C^+ (3875.68 Å) lines as a function of delay time (fixed gate width time of 20 ns) for a laser fluence of (402 J/cm^2). (b) Velocity distributions derived from the experimental TOF profiles for the indicated species.

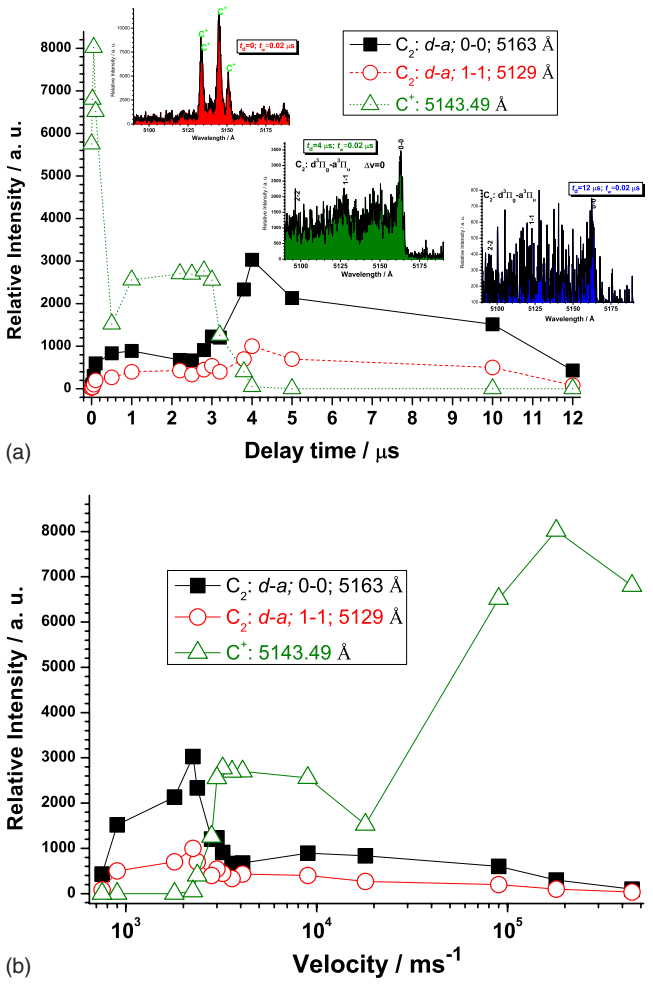

FIG. 11. (Color online) (a) Number density TOF distributions for C_2 ($d-a$; 0-0; 5163 Å), C_2 ($d-a$; 1-1; 5129 Å), and C^+ (5143.49 Å) lines as a function of delay time (fixed gate width time of 20 ns). The inset plots illustrate some spectra observed at different delay times. (b) Velocity distributions derived from the experimental TOF profiles for the indicated species.

emission tails extend up to ~4 μs. We observe the appearance of a delayed CN(B-X) very weak maximum (~10 μs) in the emission intensity. The CN(B-X) emission tail extends up to ~15 μs. The enhanced excitation at such a long time from the onset of the ablation laser pulse supports the idea that CN is mainly excited by collisions with the ablated carbon atoms and molecules with N_2 ($C_2^* + N_2 \rightarrow 2CN^*$; $C^* + N_2 \rightarrow CN^* + 1/2N_2$) . The velocity distributions of C^+ and N_2^+ ionic species are comparatively narrower than the velocity distribution of C and CN neutral species, which are nearly equal when properly scaled.

The emission intensity temporal profile or number density TOF distributions and velocity distributions for the ablation experiments induced by CO_2 laser pulses (402 J/cm^2) from C_2 ($d-a$; 0-0; 5163 Å), C_2 ($d-a$; 1-1; 5129 Å), and singly ionize carbon line at 5143.49 Å are presented in Fig. 11. The inset plots in Fig. 11(a) illustrate some spectra observed at different delay times. The electronic excitation probability in the plume is determined by the density of energetic collisions and thereby the emission intensity of C_2 at a given time and position in the plume corresponds to the density of the electronically excited molecules. However, the density also depends on processes such as down cascade and fragmentation of C_n species, with $n > 2$, in addition to collision frequency. Although the radiative emission lifetime of the $d\ ^3\Pi_g$ state is as short as ~0.1 μs,[31] the optical emission from the excited state persists even 15 μs after the arrival of the CO_2 laser pulse due to collisional excitation of molecules in the plume ($C^* + C \rightarrow C_2^*$) . The temporal evolutions of the C_2 ($d-a$; 0-0; 5163 Å) and C_2 ($d-a$; 1-1; 5129 Å) transitions show that both emissions are most enhanced at 4 μs. The enhanced excitation at such a long from the onset of the ablation laser pulse supports the idea that C_2 is not directly excited by the laser-irradiated surface but by the collisions with the ablated carbon atoms and ions and/or electrons. Thus, the temporal evolution provides information about the collision process of the carbon neutrals with the ablated species. From Fig. 11(a), we notice the appearance of a C^+ (5143.49 Å) intense maximum (~0.1 μs) and a delayed maximum (~2 μs) in the emission intensity distribution. The C^+ emission tail extends up to ~4 μs. We also observe the appearance of a C_2 ($d-a$) weak maximum (~1 μs) and a delayed intense maximum (~4 μs) in the emis-

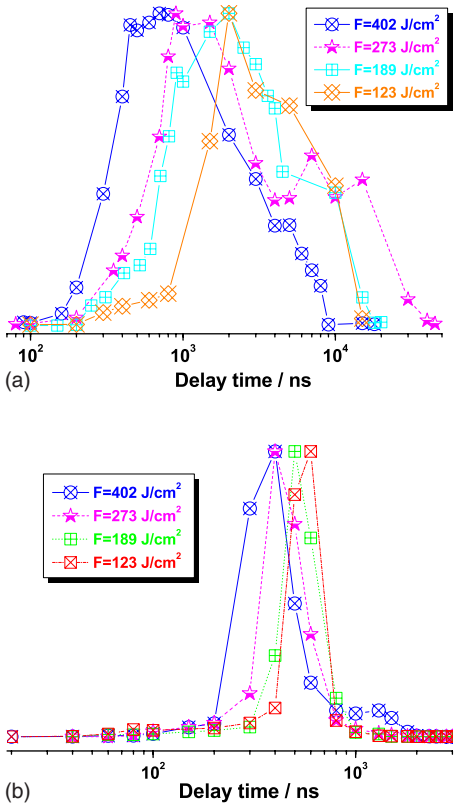

FIG. 12. (Color online) Normalized number density TOF distributions for (a) C (2478.56 Å) and (b) C^{3+} (2524.41 Å) lines for various laser fluences.

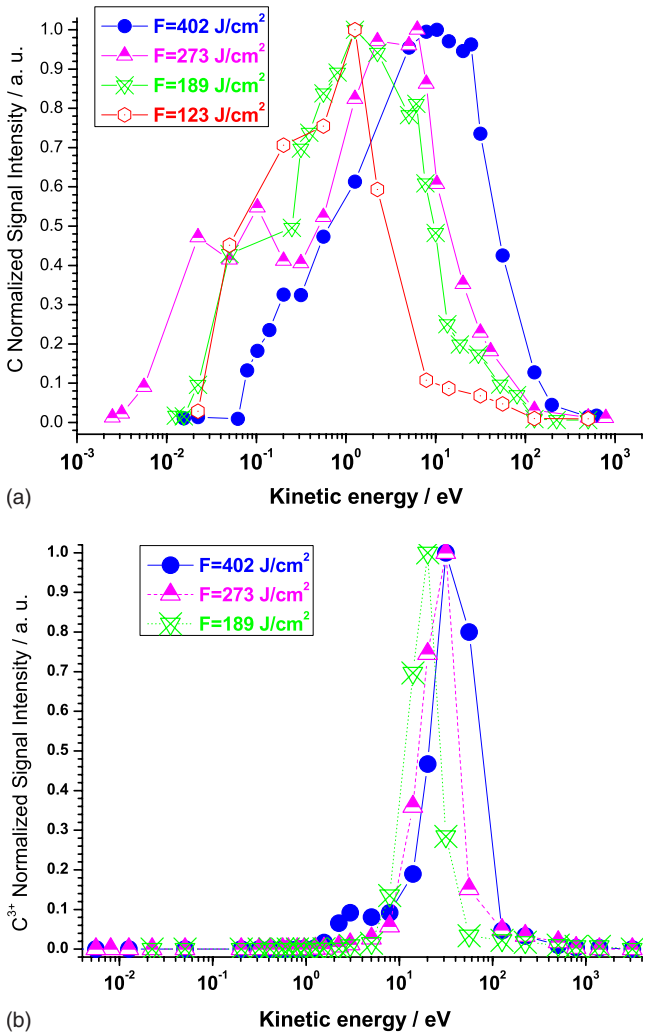

FIG. 13. (Color online) Kinetic energy distributions of (a) C (2478.56 Å) and (b) C^{3+} (2524.41 Å) lines derived from the TOF spectra (Fig. 12) for various laser fluences.

sion intensity. The C_2 $(d-a)$ emission tail extends up to ~13 μs. The velocity distributions of C^+ and C_2 $(d-a)$ show two main components, with most probable velocities of approximately 5 and 500 km/s and 3 and 9 km/s, respectively. On the other hand, the C^+ ionic species shows that their velocity distributions are peaked at ~3 and 180 km/s, higher than those corresponding to the carbon molecular species at ~2 and ~8 km/s, but much narrow.

Figure 12 presents the normalized TOF distributions for C (2478.56 Å) [Fig. 12(a)] and C^{3+} (2524.41 Å) [Fig. 12(b)] lines for various laser fluences. The TOF spectrum of emitted C neutrals, taken at high laser fluences (123–402 J cm^{-2}), was found to consist of a broad double peak [Fig. 12(a)], which maximum shifts toward higher energy as laser fluence increases. It is assumed that at higher laser fluence the plasma is more energetic and more ionized. The kinetic energy obtained from the TOF spectra is plotted in Fig. 13 for several values of the laser fluence. The results show large atomic and ion average kinetic energies. We have observed carbon atoms with kinetic energy ranging from ~0.002 up to ~500 eV, depending on the laser fluence used. For the C^{3+} (2524.41 Å) line, the kinetic energy ranges from ~1 up to ~500 eV, depending on the laser fluence used. The carbon kinetic energy shows the same overall features: a strong dependence on the laser fluence at moderate laser fluences (up to ~189 J/cm^2), followed by a slower growth, until a plateau is reached at higher fluence levels (>273 J/cm^2). Increasing of the laser fluence leads to broadening of C atoms' TOF and KE distributions [see Figs. 12(a) and 13(a)] and to the formation of a well-pronounced low-energy distribution. At laser fluences of 189 and 273 J/cm^2, the TOF and KE distributions consist of a unique population of C^{3+} ions. The temporal distribution of this kind of ions is narrow and strongly peaked, and the kinetic energy (~20 eV) is a weak function of the laser fluence. At 402 J/cm^2, the TOF and KE distributions consist of two populations of C^{3+} ions and a well-pronounced low-energy distribution (~3 eV).

C. Plasma temperature and electron density

The main factors that influence the emission by the plasma are its temperature, the number density of the emitting species (e.g., atoms, ions, molecules, etc.), and the electron density. The number density of the emitting species depends on the total mass ablated by the laser, the plasma temperature, and the degree of the excitation and/or ionization of the plasma. The vaporized amount, in turn, depends on the absorption of the incident laser radiation by the surface, the plasma shielding,[28] which is related to the electron density of the plasma, and the laser fluence. Therefore, the knowledge of the plasma temperature and the density of plasma species are vital for the understanding of the atomi-

zation, excitation, and ionization processes occurring in the plasma. For plasma in local thermodynamic equilibrium (LTE), the population density of atomic and ionic electronic states is described by a Boltzmann distribution. The conditions satisfying this assumption of LTE require the radiative depopulation rates to be negligible compared to the collisional depopulation rates. This essentially implies that an excited state must have a higher probability of de-excitation by collisions than by spontaneous emission. For optically thin plasma, the reabsorption effects of plasma emission are negligible. So, the emitted spectral line intensity is a measure of the population of the corresponding energy level of this element in the plasma. For LTE plasma, the temperature can be calculated from the relative intensities of several atomic or ionic lines by[32]

$$\ln\left[\frac{I_{ki}\lambda_{ki}}{g_k A_{ki}}\right] = C - \frac{E_k}{k_B T}, \tag{1}$$

where I_{ki} is the emissivity in W m^{-3} sr^{-1} of the emitted $k \rightarrow i$ spectral line, λ_{ki} is the wavelength, $g_k=2J_k+1$ is the statistical weight, A_{ki} is the Einstein transition probability of spontaneous emission, E_k/k_B is the normalized energy of the upper electronic level, $C=\ln[hcN_k/4\pi Q(T)]$ [$Q(T)$ is the partition function], and T is the temperature. In LTE all temperatures are assumed to be equal, i.e., $T_e \approx T_{\text{ion}} \approx T_{\text{plasma}}$. The Boltzmann method implies the assumption of LTE, but given the high electron density in our plasmas (see further), this assumption seems to be satisfied at least during the first 5 μs of the plasma lifetime. The emitted spectral line intensity from a given state of excitation can be used to evaluate the plasma temperature. By plotting the left hand side of Eq. (1) versus the excited level energy E_k, the plasma temperature can be obtained from the slope of the obtained straight line. The plasma temperature was determined from the emission line intensities of several C$^+$ lines observed in the laser-induced plasma of carbon target for a delay time of 1 μs and 0.02 μs gate width. The spectral lines' wavelengths, energies of the upper levels, statistical weights, and transition probabilities used for these lines were obtained from NIST.[33] The obtained excitation temperature was $26\,000 \pm 3000$ K. An example showing a plot of Eq. (1) and relevant parameters involved in the calculation of excitation temperature can be found in our previous paper.[26] Real plasmas provide, even in the worst cases, just an approximation to LTE. However, their spatial inhomogeneity is very large as concerns the temperature and number density distributions of the different species. Consequently, the LTE occurs only within a very small volume of the plasma.

Spectral lines are always broadened, partly due to the finite resolution of the used spectrometer and partly to intrinsic physical causes. The principal physical causes of spectral line broadening are the Doppler and Stark broadening. The Doppler broadening is due to the thermal motion of the emitting atoms or ions. For a Maxwellian velocity distribution the line shape is Gaussian, and the FWHM may be estimated as (in Å): $\Delta\lambda_{\text{FWHM}}{}^{D}=7.16\times10^{-7}\lambda(T/M)^{1/2}$, being λ the wavelength in Å, T the temperature of the emitters in K, and M the atomic mass in amu. Stark line broadening from collisions of charged species is the primary mechanism influencing the emission spectra in these experiments. The electron number density can be obtained from the Stark broadening of the emission lines. This is because Stark broadening results from Coulomb interactions between the radiator and the charged particles present in the plasma. Both ions and electrons induce Stark broadening, but electrons are responsible for the major part because of their higher relative velocities. The electrons in the plasma can perturb the energy levels of the individual ions, which broaden the emission lines originating from these excited levels. Stark broadening of well-isolated lines in the plasma is, thus, useful for estimating the electron number densities provided that the Stark broadening coefficients have been measured or calculated. The line profile for Stark broadened is well described by a Lorentzian function. Since the instrumental line broadening exhibits Gaussian shape, the Stark linewidth $\Delta\lambda_{\text{FWHM}}{}^{S}$ can be extracted from the measured linewidth $\Delta\lambda_{\text{observed}}$ by subtracting the instrumental and Doppler line broadening $\Delta\lambda_{\text{instrument}}$: $\Delta\lambda_{\text{FWHM}}{}^{S}=\Delta\lambda_{\text{observed}}-\Delta\lambda_{\text{instrument}}-\Delta\lambda_{\text{FWHM}}{}^{D}$. In our case $\Delta\lambda_{\text{instrument}}$ was 0.1 Å nm (determined by measuring the FWHM of the Cu and Ne lines emitted by a HCL). In our experiments, for C$^+$ lines, the Doppler linewidths are 0.09–0.14 Å at 26 000 K. The width of the Stark broadening spectral line depends on the electron density n_e. Both the linear and the quadratic Stark effect are encountered in spectroscopy. For a non-H-like line, the electron density n_e (in cm^{-3}) could be determined from the FWHM of the line from the approximated formula[34]

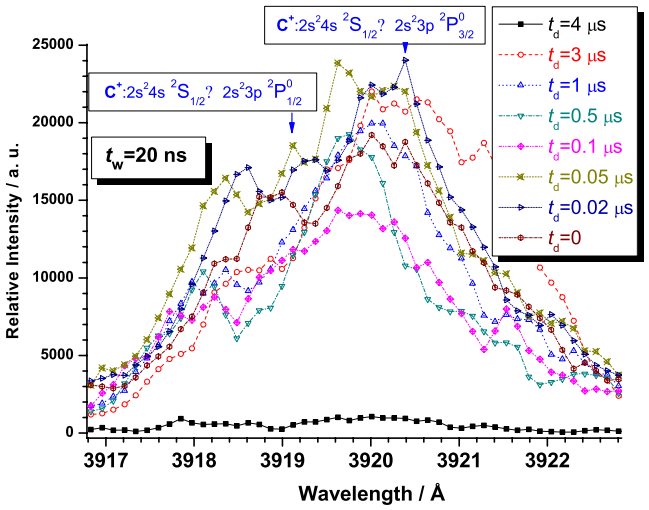

FIG. 14. (Color online) Stark-broadened profiles of the C$^+$ line at 3920 Å at different delay times for a fixed gate width time of 0.02 μs.

$$\Delta\lambda_{\text{FWHM}}^{S} = 2W\left(\frac{n_e}{10^{16}}\right), \tag{2}$$

where W is the electron-impact parameter (Stark broadening value). The carbon ionic multiplet line at ~3920 Å was identified as a candidate for electron-density measurements. Figure 14 shows the 3920 Å carbon ionic line with sufficient resolution to measure the FWHM at eight different time delays. All the data points were fitted with Lorentzian function to determine the Stark linewidth. By substituting these values in Eq. (2) and the corresponding value of Stark broadening

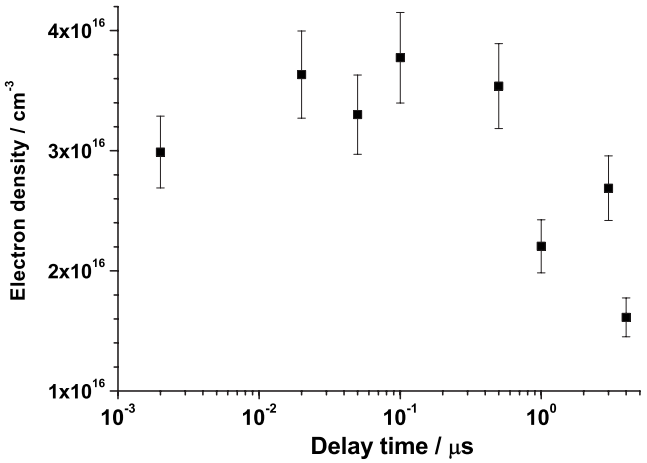

FIG. 15. The temporal evolution of electron density at different delay times from plasma ignition.

W (0.465 Å from Griem[34] at plasma temperature of 26 000 K), we obtain the electron density. Figure 15 gives the time evolution of electron density by setting the gate width of the intensifier at 0.02 μs. The initial electron density at 0.02 μs is approximately 3×10^{16} cm^{-3}. Afterwards, the density increases over the period of 0.1 μs and reaches a maximum at 0.1 μs (time of the peak of the CO_2 laser pulse), and then decrease as the time is further increased. At shorter delay times (<0.1 μs), the line to continuum ratio is small and the density measurement is sensitive to errors in setting the true continuum level. For times >0.1 μs, the line to continuum ratio is within reasonable limits and the values of electron density shown in Fig. 15 should be reliable. Initially the laser-induced plasma expands isothermically within the time of the duration of the laser pulse. After termination of the peak laser pulse (~0.1 μs) the plasma expands adiabatically. During this expansion the thermal energy is converted into kinetic energy and the plasma cools down rapidly. After 4 μs, the electron density is about 1.5×10^{16} cm^{-3}. For a long time >4 μs, subsequent decreased C^+ emission intensities result in poor signal-to-noise ratios, and there exits a limitation in the spectral resolution. The decrease in n_e is mainly due to recombination between electrons and ions in the plasma. These processes correspond to the so-called radiative recombination and three-body recombination processes in which a third body may be either a heavy particle or an electron.

In order to further identify the properties of the ablation plasma plumes originated from graphite targets, we have estimated the vibrational temperatures of C_2 molecule as function of delay time. The emission intensities of the C_2 $d-a$ swan $\Delta v=+1$ band sequence (Figs. 3 and 5) were used to estimate these vibrational temperatures T_{vib}. For a plasma in LTE, the intensity of an individual vibrational $v'-v''$ band $I_{v'-v''}$ is given by

$$\ln\left(\frac{I_{v'-v''}\lambda^4_{v'-v''}}{q_{v'-v''}}\right)=A-\frac{G(v')hc}{k_BT_{\mathrm{vib}}}, \tag{3}$$

where A is a constant, $\lambda_{v'-v''}$ is the wavelength corresponding to the band head, $q_{v'-v''}=|\int_0^\infty \Psi_{v'}(R)\Psi_{v''}(R)dR|^2$ is the Franck–Condon factor, and $G(v')hc/k_B$ is the normalized energy of the upper vibrational level v'. A linear fit of $\ln(I_{v'-v''}\lambda^4_{v'-v''}/q_{v'-v''})$ as a function of the upper normalized electronic-vibrational energies has a slope equal to $-1/T_{\mathrm{vib}}$. The estimated vibrational temperatures were $T_{\mathrm{vib}}=8000\pm500$, 8300 ± 600, 7500 ± 600, and 4500 ± 900 K at 3, 5, 10, and 15 μs after plasma ignition, respectively. These vibrational temperatures are much lower than the excitation temperature at 1 μs ($26\,000\pm3000$ K) because a few microseconds are a lot of time in the plasma evolution. As it can be seen from Fig. 5, it is very difficult to measure the intensity of the C_2 $d-a$ swan $\Delta v=+1$ band sequence at $t_d<3$ μs. The behavior of vibrational temperatures is compatible with a cooling stage.

Optical emission accompanying TEA-CO_2 nanosecond laser ablation of carbon is very long lived (~40 μs) relative to the average radiative lifetimes of the excited levels that give rise to the observed emission lines. At distances close to the target surface (<9 mm), all of the emission lines of C, C^+, C^{2+}, and C^{3+} expected in the 2000–10 000 Å wavelength range are observed,[26] illustrating that the excited species giving rise to the optical emission are produced by a nonspecific mechanism during the TEA-CO_2 laser ablation process. However, a direct excitation–de-excitation mechanism cannot explain the observed emission spectra. Electron-impact ionization would explain the emission intensity variation with the time for C, C^+, C^{2+}, C^{3+}, and C_2 species. On the other hand, the formation of the excited molecular species would happen in gas phase by collisions between atomic or ionic species present in the plume and the residual gas at times far away from the plasma ignition. The emission process at this plasma stage is divided into two different processes associated, respectively, with the shock formation and the plasma cooling. During the former, the atoms, molecules, and ions gushing out from the carbon target are adiabatically compressed against the surrounding gas. During the latter stage the temperature of the plasma and consequently the emission intensities of the atomic lines and molecular bands decrease gradually.

The evolution of the TEA-CO_2 laser-induced carbon plasma can be divided into several transient phases. The initial plasma ($t_d<2$ μs) is characterized by high electron and ion densities [$(1-4)\times10^{16}$ cm^{-3}], and temperatures around 2.2 eV. The emission spectrum from this early stage is characterized by emission lines from C^{3+}, C^{2+}, and C^+ ions. Owing to the high electron density, the emission lines are broadened by Stark effect. The ionic species (C^{3+}, C^{2+}, C^+, and N_2^+) decay rapidly being observed up to ~3 μs. Emission lines from C atoms and molecular species (C_2, CN, CH, and OH) in excited electronic states can be found after about 0.3 μs time delay. As the plasma expands and cools, the electrons and ions recombine. After the initial plasma ($t_d>3$ μs), the molecular emissions increase slowly up to ~5 μs and after that decay slowly up to ~40 μs.

IV. CONCLUSION

High density plasma created by CO_2 laser pulses in graphite at $\lambda=10.591$ μm in a medium-vacuum atmosphere

(4 Pa) has been investigated by spectroscopic measurements in UV-vis-NIR spectral range. The investigation has been carried out in a regime of relatively high laser fluences ($123-402$ J/cm^2). The emission observed at 9.0 mm from the target is due to the relaxation of excited atomic C, N, O, and H; ionic fragments C^+, C^{2+}, C^{3+}, and C^{4+}; and molecular bands of C_2, CN, OH, CH, and N_2^+. The characteristics of the spectral emission intensities for some species have been investigated as a function of the delay time after the plasma formation. The velocity and kinetic energy distributions for different species were obtained from TOF measurements using time-resolved optical emission spectroscopy. All the ionic lines follow the time profile of the laser pulse lasting until 3 or 4 μs. A different behavior of atomic C and molecular species can be observed, possibly due to the tail of the pulse and the continuous recombination of ions with electrons to give excited carbon. Taking into account the number density TOF distributions of neutral carbon and its ionic species, we suggest that the ionic species come from the ionization of the neutral C formed at the target surface by the initial part of the laser pulse. Decreasing of the laser fluence will drive to a weaker plume formation and consequently to a decrease in its absorption and screening off of the target from the later part of the pulse. At low laser fluences, we think that we are detecting ionic species formed both at the target surface and in the nascent plume. The temperature measurements have been performed by Boltzmann diagram method using C^+ lines, while electron-density estimations were made using the Stark broadening method. Time-resolved studies of electron density and temperatures have been carried out using emission lines of C^+. Estimates of vibrational temperatures of C_2 electronically excited species at various times after plasma formation are made. The formation of excited molecular species is produced in gas phase by collisions between atomic or ionic species present in the plume and the residual gas, at times far away from the plasma formation ($t_d > 0.4$ μs).

ACKNOWLEDGMENTS

We gratefully acknowledge the support received in part by the DGICYT (Spain) Project Nos. MEC: CTQ2007-60177/BQU and MEC: CTQ2008-05393/BQU for this research.

[1]H. W. Kroto, J. R. Heath, S. C. O'Brien, R. F. Curl, and R. E. Smalley, Nature (London) **318**, 162 (1985).
[2]W. Kratschmer, L. D. Lamb, F. Fostiropoulos, and D. R. Huffman, Nature (London) **347**, 354 (1990).
[3]H. Koinuma, M. S. Kim, T. Asakwa, and M. Yoshimoto, Fullerene Sci. Technol. **4**, 599 (1996).
[4]J. Bulir, M. Novotny, M. Jelinek, J. Lancok, Z. Zelinger, and M. Trchova, Diamond Relat. Mater. **11**, 1223 (2002).
[5]T. Ikegami, F. Nakanishi, M. Uchiyama, and K. Ebihara, Thin Solid Films **457**, 7 (2004).
[6]M. N. R. Ashfold, F. Claeyssens, G. M. Fuge, and S. J. Henley, Chem. Soc. Rev. **33**, 23 (2004).
[7]G. Meijer and D. S. Bethane, J. Chem. Phys. **93**, 7800 (1990).
[8]C. Wulker, W. Theobald, and F. P. Schafer, Phys. Rev. E **50**, 4920 (1994).
[9]Z. Andreic, D. Gracin, V. Henc-Bartilic, H. J. Kunze, F. Ruh, and L. Aschke, Phys. Scr. **53**, 339 (1996).
[10]S. S. Harilal, R. C. Issac, C. V. Bindhu, V. P. N. Nampoori, and C. P. G. Vallabhan, Jpn. J. Appl. Phys., Part 1 **36**, 134 (1997).
[11]A. V. Demyanenko, V. S. Letokhov, A. A. Puretskii, and E. A. Ryabov, Quantum Electron. **27**, 983 (1997).
[12]K. H. Wong, T. Y. Tou, and K. S. Low, J. Appl. Phys. **83**, 2286 (1998).
[13]J. Hermann, C. Vivien, A. P. Carricato, and C. Boulmer-Leborgne, Appl. Surf. Sci. **129**, 645 (1998).
[14]C. Vivien, J. Hermann, A. Perrone, C. Boulmer-Leborgne, and A. Luches, J. Phys. D **31**, 1263 (1998).
[15]S. Arepalli, P. Nikolaev, W. Holmes, and C. D. Scott, Appl. Phys. A: Mater. Sci. Process. **69**, 1 (1999).
[16]Y. K. Choi, H. S. Im, and K. W. Jung, Bull. Korean Chem. Soc. **20**, 1501 (1999).
[17]S. M. Park and K. H. Lee, Appl. Surf. Sci. **178**, 37 (2001).
[18]S. Acquaviva and M. L. Giorgi, J. Phys. B **35**, 795 (2002).
[19]T. Sakka, K. Saito, and Y. H. Ogata, Appl. Surf. Sci. **197**, 246 (2002).
[20]S. Abdelli-Messaci, J. T. Kerdja, A. Bendib, and S. Malek, J. Phys. D: Appl. Phys. **35**, 2772 (2002).
[21]C. S. Ake, H. Sobral, E. Sterling, and M. Villagran-Muniz, Appl. Phys. A: Mater. Sci. Process. **79**, 1345 (2004).
[22]H. S. Park, S. H. Nam, and S. M. Park, J. Appl. Phys. **97**, 113103 (2005).
[23]W.-O. Siew, K. H. Wong, S. S. Yap, and T. Y. Tou, IEEE Trans. Plasma Sci. **33**, 176 (2005).
[24]Z. S. Gong, J. Sun, N. Xu, Z. F. Ying, Y. F. Lu, D. Yu, and J. D. Wu, Diamond Relat. Mater. **16**, 124 (2007).
[25]E. Vors, C. Gallou, and L. Salmon, Spectrochim. Acta, Part B **63**, 1198 (2008).
[26]J. J. Camacho, L. Diaz, M. Santos, D. Reyman, and J. M. L. Poyato, J. Phys. D **41**, 105201 (2008).
[27]J. J. Camacho, M. Santos, L. Díaz, and J. M. L. Poyato, Appl. Phys. A: Mater. Sci. Process. **94**, 373 (2009).
[28]B. Le Drogoff, J. Margot, M. Chaker, M. Sabsabi, O. Barthélemy, T. W. Johnston, S. Laville, F. Vidal, and V. Y. Kaenel, Spectrochim. Acta, Part B **56**, 987 (2001).
[29]M. Rossa, C. A. Rinaldi, and J. C. Ferrero, J. Appl. Phys. **105**, 63306 (2009).
[30]K. Kagawa and S. Yokoi, Spectrochim. Acta, Part B **37**, 789 (1982).
[31]S. Arepalli, C. D. Scott, P. Nikolaev, and R. E. Smalley, Chem. Phys. Lett. **320**, 26 (2000).
[32]V. N. Rai and S. N. Thakur, in *Laser-Induced Breakdown Spectroscopy*, edited by J. P. Singh and S. N. Thakur (Elsevier, Amsterdam, 2007).
[33]NIST Atomic Spectra Database online at http://physics.nist.gov/PhysRefData/ASD/index.html.
[34]H. R. Griem, *Spectral Line Broadening by Plasmas* (Academic, New York, 1974).